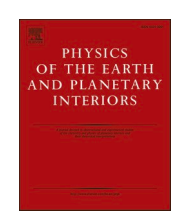
ELSEVIER

Contents lists available at ScienceDirect

Physics of the Earth and Planetary Interiors

journal homepage: www.elsevier.com/locate/pepi





Variable distribution of subducted oceanic crust beneath subduction regions of the lowermost mantle

Mingming Li

School of Earth and Space Exploration, Arizona State University, Tempe, AZ 85287-6004, USA

ARTICLE INFO

Keywords:
Mantle convection simulation
Subducted slab
Subducted oceanic crust
Lowermost mantle
Seismic heterogeneities

ABSTRACT

Subducted oceanic crust (SOC) is one of the major sources of chemical heterogeneity in Earth's mantle. Previous geodynamic modeling studies have shown that SOC in the lowermost mantle could segregate from subducted slabs and accumulate on the core-mantle boundary (CMB). However, previous models are often simplified in a variety of ways that hinder a comprehensive understanding of the dynamics of SOC in the lowermost mantle. Here, I perform 3D high-resolution geodynamic models with single-sided subduction to study the dynamics of SOC in the lowermost mantle, with a focus on regions beneath subduction zones outside the large-low velocity provinces (LLVPs). I find that the ability of a thin (\sim 10 km) SOC to segregate from the slab is greatly controlled by the morphology of the slab. The segregation of SOC is much more efficient when the slab in the lowermost mantle is folded backward and extends beneath the subducting plate with allows the SOC to directly face or contact the CMB, than when the slab extends beneath the overriding plate with the SOC at the shallowest portion of the slab. The changes of slab morphology cause strong temporal and spatial variations in the distribution of SOC (1) at the CMB, (2) within 50 km above the CMB, and (3) at \sim 50–300 km above the CMB, which, together with its variable degrees of mixing with other mantle materials, may explain the variations of seismic velocities, density, size, shape, and distribution of seismic anomalies in the lowermost mantle outside the LLVPs.

1. Introduction

Oceanic crust is produced at mid-ocean ridges and subducted to the deep mantle at subduction zone. Subducted oceanic crust (SOC) is one of the major sources of chemical heterogeneities in the deep mantle (e.g., Hofmann and White, 1982; Christensen and Hofmann, 1994; Tolstikhin and Hofmann, 2005; Li, 2021). The distribution and advection of SOC in the deep mantle are important for understanding deep mantle seismic structures, the geochemistry of volcanic rocks on Earth's surface, deep mantle dynamics, and Earth's chemical evolution.

Mineral physics experiments have shown that after being transformed to eclogite at ~50 km depth, the SOC becomes intrinsically denser than pyrolite mantle at most mantle depths (except the uppermost lower mantle where the SOC may be intrinsically less dense) (e.g., Ringwood and Irifune, 1988; Kesson et al., 1994; Hirose et al., 2005; Ricolleau et al., 2010; Tsuchiya, 2011). The possibility for the SOC to segregate and accumulate on the CMB has been explored using geodynamic models (e.g., Gurnis, 1986; Christensen and Hofmann, 1994; Brandenburg and van Keken, 2007; Davies, 2008; Tackley, 2011; Li and McNamara, 2013; Nakagawa and Tackley, 2014). It is found that, in

general, a thicker and denser SOC is easier to segregate from subducted slabs and accumulate at the core-mantle boundary (CMB) (see review by Li, 2021).

Previous geodynamic modeling studies on subducted slab dynamics in the lowermost mantle employed several simplifications, including the use of 2D and/or Cartesian geometry, double-sided subduction, low convection vigor, low model resolution, simulation of comb-like cold drippings as opposed to sheet-like strong plates, and artificial imposition of slabs in the lower mantle as initial conditions without accounting for continuous slab subduction. These model simplifications hinder a more comprehensive understanding on the advection, distribution, and dynamics of SOC in the lowermost mantle. For example, in 2D models (Christensen and Hofmann, 1994; Brandenburg and van Keken, 2007; Li and McNamara, 2013), a subducted slab does not have a third dimension. As a result, the slab morphology is over-simplified, with no characterization of dynamics at slab margins (i.e., in the 3rd dimension). In Cartesian models (e.g., Christensen and Hofmann, 1994; Lowman et al., 2004), the size and shape of thermal anomalies and chemical accumulations on the CMB and perhaps the mantle dynamics are unrealistic. In models with double-sided subduction (e.g., Li and McNamara, 2013;

E-mail address: mingming.li@asu.edu.

Mulyukova et al., 2015), the SOC is sandwiched by cold and strong slabs, causing unrealistic resistance for crustal segregation. Models with low vigor of convection overestimate the thickness of the basal thermal boundary layer (TBL) and the size of thermal anomalies on the CMB, which may also cause unrealistic crustal segregation in the lowermost mantle (e.g., Christensen and Hofmann, 1994). Models with low spatial resolution (e.g., Huang and Davies, 2007) do not capture the full dynamics of a thin oceanic crust. Slabs have been simulated as cold drippings in some 3D spherical models (e.g., Davies and Davies, 2009; Li, 2020), which are different than the more sheet-like plates thought to exist in the Earth. In the 3D models by Tackley (2011), a slab consisting of a 30 km thick layer of oceanic crust on its top layer was initially introduced in the lowermost mantle. By imposing slabs in the lower mantle as initial condition, the results are determined and thus biased by the initial model setup when the thermal structures and mantle flow field are not fully developed yet (Tackley, 2011).

The distribution of subducted oceanic crust in the lowermost mantle is closely related to observations of seismic anomalies in this depth range. Seismic observations have revealed two large-low velocity provinces (LLVPs) in the lowermost mantle beneath Africa and the central Pacific Ocean (e.g., Li and Romanowicz, 1996; Grand, 2002; Ritsema et al., 2004; Garnero et al., 2016). The LLVPs are generally interpreted as having higher temperature and likely different composition than the surrounding mantle (see review by McNamara, 2019). Surrounding the LLVPs are regions with generally higher-than-average seismic velocities. It has been observed that while some subducting slabs directly penetrate deeply into the lower mantle (e.g., Grand et al., 1997; Fukao and Obayashi, 2013), other slabs appear to be laterally deflected or flattened in the depth range of ~600-1000 km (Li et al., 2008; Fukao et al., 2009; Ritsema et al., 2011; Fukao and Obayashi, 2013). However, geodynamic modeling studies have shown that the flattened slabs may eventually sink to the deep lower mantle (e.g., Yoshioka and Naganoda, 2010; Čížková and Bina, 2019; Wang and Li, 2020). Therefore, regions in the lowermost mantle outside the LLVPs are often interpreted as being greatly influenced by ancient, relatively cold, subducted slabs.

Importantly, the regions outside the LLVPs in the lowermost mantle contain seismic heterogeneities with large variations in size, shape, seismic velocities, and density, such as (1) the widespread ultra-low velocity zones (ULVZs) that are 10s km thick and 100 s to >1000 km long, with a S wave velocity (Vs) reduction up to 50%, a P wave velocity (Vp) reduction up to 25%, a density increase up to 20%, and a variety of shapes (see review by Yu and Garnero, 2018), (2) the low velocity anomalies with moderate reduction of seismic velocities ($<\sim$ 10%) and a variety of shape and size (Sun et al., 2013; He et al., 2014; Suzuki et al., 2016; Borgeaud et al., 2017; Nelson and Grand, 2018), and (3) the seismic scatterers that are a few km in size and widely distributed in the lowermost 300 km of the mantle (e.g., Frost et al., 2017). The widespread seismic heterogeneities in Earth's lowermost mantle have been summarized in several previous studies (McNamara et al., 2010; Garnero et al., 2016; Yu and Garnero, 2018; McNamara, 2019; Li, 2020, 2021; Hansen et al., 2023), but their origin remains unclear, which is critical for unveiling the mysteries about Earth's thermal and chemical structure, dynamics, and evolution.

Recently, I found that hot thermal anomalies can form outside the LLVPs in subduction regions of the lowermost mantle, particularly when the subducted slabs are thermally heterogeneous or contain gaps (Li, 2020). However, seismic anomalies outside the LLVPs may also be caused by chemical heterogeneities. A major source of chemical heterogeneities in the subduction regions of the lowermost mantle is the SOC (e.g., Christensen and Hofmann, 1994; Tackley, 2011; Jones et al., 2020; Li, 2021; Li and McNamara, 2022; Hansen et al., 2023). In this study, 3D high-resolution spherical models with single-sided subduction are performed to study the dynamics and distribution of a thin SOC in the lowermost mantle outside the LLVPs.

2. Methods

The following dimensionless conservation equations of mass, momentum and energy are solved under the Boussinesq approximation:

$$\nabla \bullet \overrightarrow{\mathbf{u}} = 0 \tag{1}$$

$$-\nabla P + \nabla \bullet (\eta \dot{e}) + \left[Ra \left(T - \sum_{i} B_{i} C_{i} \right) + Ra_{p} \Gamma \right] \hat{\mathbf{r}} = 0$$
 (2)

$$\frac{\partial T}{\partial t} + (\overrightarrow{\mathbf{u}} \bullet \nabla)T = \nabla^2 T + H \tag{3}$$

where \overrightarrow{u} is the velocity, P is the dynamic pressure, η is the viscosity, \dot{e} is the strain rate tensor, T is temperature, \widehat{r} is unit vector in radial direction, B_i and C_i are the buoyancy number and the fraction of composition for the ith compositional component, t is time, and H is internal heating rate. Ra_p and Γ are the phase transition Rayleigh number and the phase function, respectively. Eq. (1)–(3) are solved using the finite element code CitcomCU (Zhong, 2006).

The Rayleigh number Ra is defined as:

$$Ra = \frac{\rho_0 g \alpha \Delta T R^3}{\kappa n_0},\tag{4}$$

where ρ_0 , g, α , κ and η_0 and are the reference density (which is the background mantle density), gravity acceleration, thermal expansivity, thermal diffusivity, and reference viscosity, respectively. R is the radius of the Earth. ΔT is the reference temperature which equals to the temperature increase from the surface to the CMB. Note that the Rayleigh number is defined using the radius of the Earth, which is $\sim \! 11$ times of that defined using mantle thickness. The physical parameters used in this study are summarized in Table 1.

The mantle dynamics is simulated in a regional 3D spherical-shell model domain, covering the entire mantle depth with a non-dimensional radius ranging from 0.55 at the CMB to 1.0 at the surface (Fig. 1a). The model domain has a longitudinal range of $0-120^{\circ}$, and a co-latitudinal range of $90-150^{\circ}$ (or a latitudinal range of $0-60^{\circ}$ S). There are 384 elements in the radial direction. Since I am interested in the lowermost mantle dynamics, the grid is gradually refined to have a radial resolution of 5 km in the lowermost 600 km of the model domain. There are 768 and 256 elements in the longitudinal and co-latitudinal directions, respectively, resulting in a longitudinal resolution of \sim 9.5 km and a latitudinal resolution of \sim 14.5 km near the CMB.

Generating Earth-like plates with single-side subduction is a long-standing challenge in geodynamic modeling experiments (e.g., King et al., 1992; Tackley, 2000; Lowman, 2011; Crameri and Tackley, 2015). In this study, I use similar techniques as previous work. As shown in Fig. 1b, the top surface is divided into an overriding plate and a subducting plate. The subducting plate is defined in regions at longitudes of $60-108.5^{\circ}$ and latitudes of $-20^{\circ}-0^{\circ}$. Outside the subducting plate is the overriding plate. The subducting plate has a dimensionless temperature of 0.0 and a westward angular velocity of 3 cm/yr, whereas the overriding plate has a dimensionless temperature of 0.6 (which is same as initial mantle temperature) and zero velocity. The increased

Table 1 Physical parameters used in this study.

Parameters	Reference value
Earth's radius R	6371 km
CMB radius	3481 km
Reference density ρ_0	3300 kg/m^3
Gravitational acceleration g	9.8 m/s^2
Thermal expansivity α	$1.0 \times 10^{-5} \ \mathrm{K}^{-1}$
Surface thermal diffusivity κ	$1.0 \times 10^{-6} \text{ m}^2/\text{s}$
Temperature change across the mantle ΔT	2500 K
Reference viscosity η_0	$1.0\times 10^{21}~Pa~s$

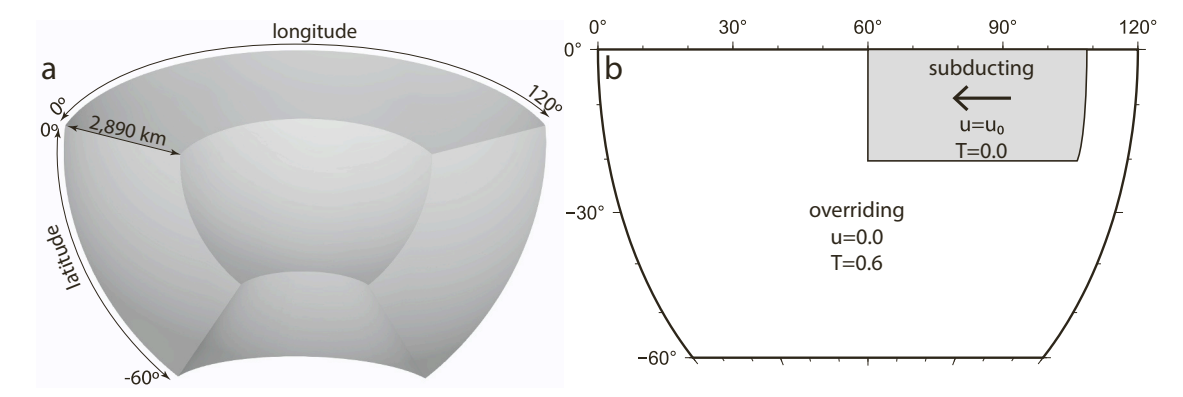


Fig. 1. a, the computational domain. b, the surface temperature and velocity boundary conditions. The gray are show the subducting surface and the white area shows the overriding surface. u_0 =3.0 cm/yr is the imposed velocity for the subducting plate.

temperature of the overriding plate is to simulate the temperature at the base of the continental lithosphere. This treatment of surface temperature boundary condition has been used before by Tan et al. (2002) and Huang and Davies (2007), which helps decouple subducted slabs from the overriding plate. Except the top surface, all other boundaries are free-slip. The side boundaries are insulating and the CMB has a fixed temperature of T=1.0 for most cases. The initial temperature is 0.6 in the model domain with small perturbations.

A layer of oceanic crust followed by a layer of depleted lithosphere are continuously introduced in regions beneath the subducting plate throughout the model run. The oceanic crust consists of purely midocean ridge basalt (MORB). The depleted lithosphere is a mixture of harzburgite and background mantle materials with the concentration of harzburgite decreasing linearly from 100% to 0% from the top to the bottom of the depleted lithosphere. The reducing harzburgite concentration with depth simulates the decreasing degree of melting with depth. The compositional density anomaly $\Delta \rho$ with respect to the background mantle is represented by a dimensionless buoyancy number as:

$$B_i = \frac{\Delta \rho_i}{\rho_0 \alpha \Delta T} \tag{5}$$

where the subscript i is varied such that B_c and B_h represent the buoyancy numbers for MORB (or oceanic crust) and harzburgite, respectively. The oceanic crust is 10 km thick, and the depleted lithosphere is 100 km thick. I use B_c =0.8 and B_{hz} = -0.16, corresponding to intrinsic density anomalies of 2% and -0.4%, respectively.

The compositional field is advected with tracers. I use the absolute tracer method to simulate the advection of the compositional fields (Tackley and King, 2003). Note that for the same model resolution, the ratio tracer method can handle chemical diffusion better than the absolute tracer method (Tackley and King, 2003). However, besides different tracer methods, the accuracy of chemical advection is also greatly (and is likely more) controlled by model resolution. Compared to the ratio tracer method, the absolute tracer method requires a significantly smaller number of tracers and allows to perform simulations with as high resolution as possible.

Following (Tackley and King, 2003), the fraction of the ith compositional component C_i in each element of the model domain is computed by:

$$C_i = \frac{AN_i}{V_e} \tag{6}$$

where N_i is the number of tracers in the element for the ith compositional component, V_e is the volume of the element, and A is a constant equal to the average volume that a tracer 'carries' and is defined as:

$$A = \frac{V_{total}}{N_{ave} \times N_{el}} \tag{7}$$

where V_{total} and N_{ave} are respectively the volume and the number of elements of the entire model domain, and N_{ave} is the average number of tracers per element which is 30 in this study. As found by Tackley and King (2003), due to statistical fluctuation in N_i and settling of tracers, it is possible that one element is filled with too many tracers such that the summation of C_i is >1. In such situation, the C_i is truncated to C_i^{tr} by:

$$C_i^{tr} = \frac{C_i}{\sum_i C_i} \tag{8}$$

All side boundaries are free-slip and insulating. To avoid the unrealistic accumulations of subducted oceanic crust at the side boundaries, tracers that are advected to regions within 2° from side boundaries are removed from the model domain. This study thus focuses on the distribution of subducted oceanic crust away from side boundaries.

The viscosity is both temperature- and depth-dependent, and in some cases, it also depends on the presence of post-Perovskite (pPv) phase. I use the Frank-Kamenetskii viscosity law (Frank-Kamenetskii, 1969) as:

$$\eta = \eta_r exp[A(0.6 - T)] \tag{9}$$

where A is the dimensionless activation energy, and the prefactor η_r is 1.0 in the upper mantle and 30.0 in the lower mantle. I use A=6.91 in hot regions with T \geq 0.6 and A=11.51 in cold regions with T<0.6 in most cases. The advantage of using different activation energy between hot and cold regions is that the viscosity of subducted slabs can be varied model-to-model without affecting the plume viscosity, which enables us to isolate the effects of slab viscosity on the results.

Some models include the Bridgmanite (Bdg) to pPv phase transition which is simulated by using a phase function Γ defined as:

$$\Gamma(\pi) = 0.5 + 0.5 \tanh\left(\frac{\pi}{w}\right) \tag{10}$$

where w= 0.0094 is the width of the phase transition and π is the excess pressure which is defined as:

$$\pi = r_{ppv} - r - \gamma \left(T - T_{ppv} \right) \tag{11}$$

where r is the radius, (r_{ppv} =0.5762, T_{ppv} =0.50) is a point on the phase boundary, and γ =0.12 is the Clapeyron slope equivalent to 10 MPa/K which roughly agrees with that constrained by mineral physics studies (Shim, 2008). The phase transition Rayleigh number is defined as:

$$Ra_{p} = \frac{\Delta \rho_{ppv}}{\rho \alpha_{0} \Delta T} Ra \tag{12}$$

where $\Delta\rho_{pp\nu}$ is the density change due to the pPv phase transition. In

models with pPv phase transition, the viscosity law is modified as:

$$\eta = \eta_r exp \left[A(0.6 - T) + \Gamma \ln(\eta_{ppv}) \right]$$
(13)

where η_{ppv} is the magnitude of the viscosity jump due to the pPv phase transition.

3. Results

I define case 1 as the reference case. In this case, the Rayleigh number is $Ra=2\times10^8$, and the activation coefficient is A=11.51 in cold regions. The model starts with a homogeneous internal temperature of T=0.6 (with small perturbations), and a cold slab with 10-km-thick oceanic crust on its topmost layer is consistently subducted to the lowermost mantle.

The time evolution of the temperature and compositional fields of case 1 is shown in Supplementary Information Movie S1. After initial condition, the subducted slab sinks nearly vertically into the deep mantle. As the subducted slab approaches the CMB, it is advected laterally toward the west side boundary (Supplementary Information Movie S1). The average non-dimensional temperature in the mantle (excluding the top and basal TBLs), as shown in Fig. 2a, is ~ 0.55 with a standard deviation of ~ 0.05 . As shown in Fig. 2b, the average viscosity is $\sim 1.2 \times 10^{21}$ Pa s in the upper mantle (except the top TBL). It increases to $\sim 3.5 \times 10^{22}$ at the top of the lower mantle and further increases with depth, reaching a maximum value of about 1.2×10^{23} Pa s at ~ 2700 km depth (Fig. 2b). After that it decreases with depth (Fig. 2b). The viscosity structure in this model generally agrees with that constrained through geoid inversion (e.g., Steinberger and Calderwood, 2006). The depth profile of the viscosity shows a large standard deviation (Fig. 2b) because the viscosity in the model strongly depends on temperature. The subducted slab reaches its maximum sinking speed of ~1.2 cm/yr in the uppermost lower mantle and subsequently decreases with depth to ~ 0.3 cm/yr in the lowermost mantle (Fig. 2c), where it experiences lateral deflection (Supplementary Information Movie S1).

At 711 Myr, the subducted slab extends laterally beneath the overriding plate, with the SOC located at the shallowest portions of the slab and without making contact with the CMB (Fig. 3a-c). At this time, only a small portion of the SOC is segregated on the CMB near the west boundary where upwelling plumes form and the subducted slab is warmed up.

From \sim 711 to 870 Myr, the most recent subducted portion of the slab in the lowermost mantle undergoes overturning and is advected eastward beneath the subducting plate (Fig. 3d). The associated SOC is gradually turned over to the deepest portions of the slab (Fig. 3f), and some of it segregates and falls onto the CMB (Fig. 3e).

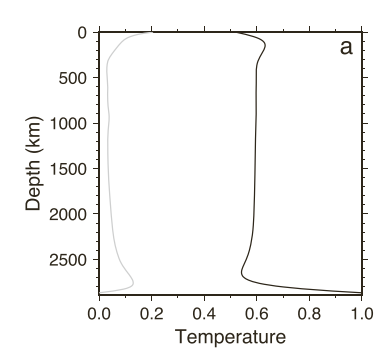
After \sim 870 Myr, the most recent subducted portion of the slab in the lowermost mantle is advected toward the west boundary once again (Fig. 3g), with SOC once again present in the shallowest portion of the slab (Fig. 3i). In contrast, the portion of the subducted slab beneath the subducting plate warms up, and the majority of the associated SOC segregates onto the CMB (Fig. 3h). The region near the southern margin

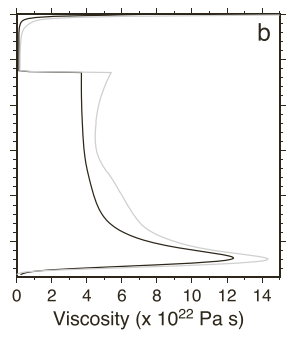
of the subducted slab in the lowermost mantle contains the largest amount of segregated oceanic crust on the CMB (e.g., Fig. 3g). After reaching the CMB, the SOC is advected laterally toward the side boundaries and is eventually removed from the model domain (Supplementary Information Movie S1). While migrating along the CMB, the SOC is collected, dispersed, and shaped into a variety of different morphology with variable degrees of mixing with the background mantle material and subducted depleted lithosphere material (Fig. 3h, Supplementary Information Movie S1).

I further quantify the distribution of SOC in the lowermost mantle. At each depth, I calculate the area of regions where the fraction of SOC is larger than 0.5, which is then divided by the area of the model domain at that depth to obtain the areal fraction, denoted as F_c . Fig. 4a presents the depth profile of F_c as a function of time for case 1. After the initial condition at ~300 Myr, the SOC starts to reach the lowermost 300 km of the mantle. Between ~300 and 850 Myr, the majority of SOC exists within a depth range of approximately 100 to 300 km above the CMB. After ~850 Myr, the SOC starts to segregate on the CMB. During ~900–1200 Myr, the SOC is mostly concentrated in the lowermost 50 km of the mantle, and as shown in Fig. 4b, the F_c at the CMB increases significantly from approximately 1% to 21% during this time (Fig. 4b). Subsequently, the F_c at the CMB decreases to around 9% (Fig. 4b) at 1400 Myr due to the ongoing removement of crustal materials at side boundaries of the model domain.

Case 2 uses a lower activation energy of A=4.61 for cold regions which results in reduction of viscosity contrast between slab and the surrounding mantle. Different from case 1, the subducted slab in the lowermost mantle keeps moving to the west of the model domain beneath the overriding plate (Supplementary Information Movie S2. Fig. 5a-c). As a result, the SOC always remains in the shallowest part of the slab and never directly contacts the CMB. Only when the slab in the lowermost mantle is warmed up near the west boundary does a small amount of SOC segregate to the CMB (Supplementary Information Movie S2). The majority of SOC exists within a range of approximately 50 to 300 km above the CMB (Fig. 5d), and only a maximum of 4% of CMB area is covered by crustal materials at approximately 1100 Myr (Fig. 5e).

Case 3 incorporates the pPv phase transition in the lowermost mantle and there is a $100\times$ viscosity reduction for the pPv phase with $\eta_{ppv}=0.01$, whereas other parameters are the same as case 1. The pPv phase occurs in relatively cold regions of the lowermost mantle, leading to a significant reduction of viscosity. This viscosity reduction causes an increase in the slab sinking rate in the deep mantle (Fig. 2c, dashed curve) and results in a reduced thickness of the slab compared to case 1. The slab in the lowermost mantle is also heated up faster than in case 1. No slab folding is observed in the lowermost mantle and the slab extends laterally only in the west direction beneath the overriding plate with the SOC always at the shallowest portion of the slab (Supplementary Information Movie S3). Although the subducted slab in the lowermost mantle has reduced viscosity due to the pPv phase, the SOC does not penetrate through the slab and contacts the CMB (Fig. 6a-c). Most SOC exists at a depth of \sim 50–300 km above the CMB (Fig. 6d), and there is





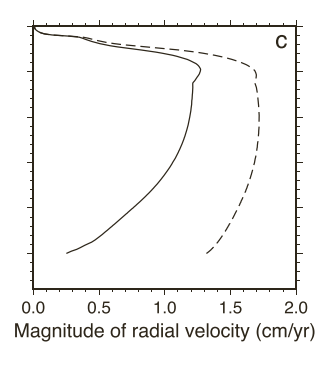


Fig. 2. Depth profiles of the average temperature (a) and the average viscosity (b) of the mantle, and the magnitude of radial velocity within the subducted slab (c, solid curve) for case 1 at 711 Myr. The gray curves in panels (a) and (b) show the associated standard deviations, and the dashed curve in panel (c) shows the average magnitude of the radial velocity within the subducted slab in case 3 at 1013 Myr. Subducted slabs are defined in regions where the non-dimensional temperature is <0.435.

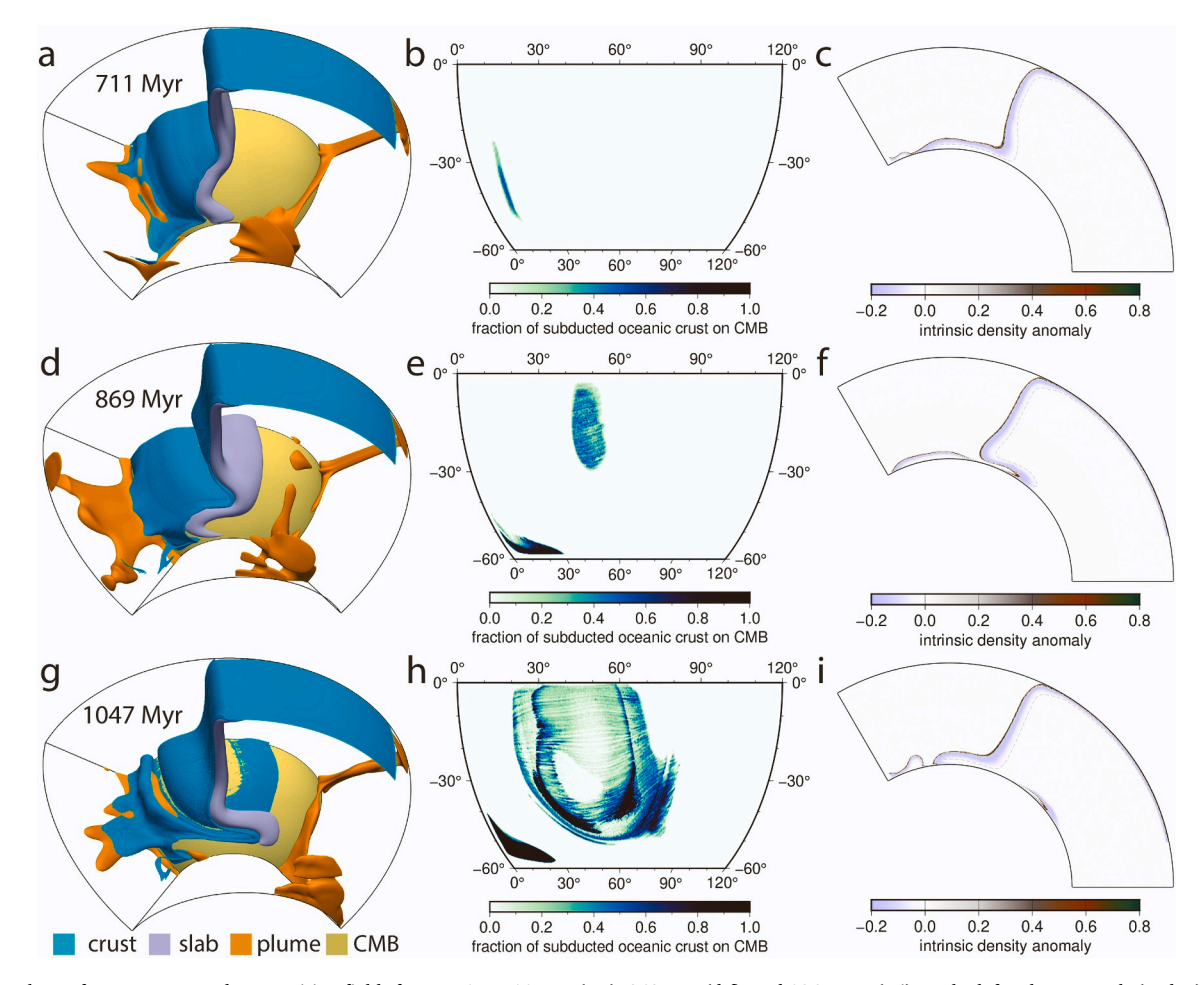


Fig. 3. Snapshots of temperature and composition fields for case 1 at 711 Myr (a-c), 869 Myr (d-f), and 1047 Myr (g-i). In the left column panels (a, d, g), cyan color shows regions where the fraction of oceanic crust is larger than 0.3, blueish color shows a subducted slab by the temperature isosurface of T=0.435, orange color shows mantle plumes as the isosurface of the temperature anomaly (after removing the lateral average temperature) at 0.15, and green color shows the CMB. The middle column panels (b, e, h) show the fraction of SOC on the CMB. The right column panels (c, f, i) show the vertical cross-sections of the intrinsic density anomaly at a latitude of -10° , with brown to green colors showing regions concentrated with SOC and blue color showing regions with depleted lithosphere, and gray dashed curves showing the subducted slab as the temperature contour at T=0.435. (For interpretation of the references to color in this figure legend, the reader is referred to the web version of this article.)

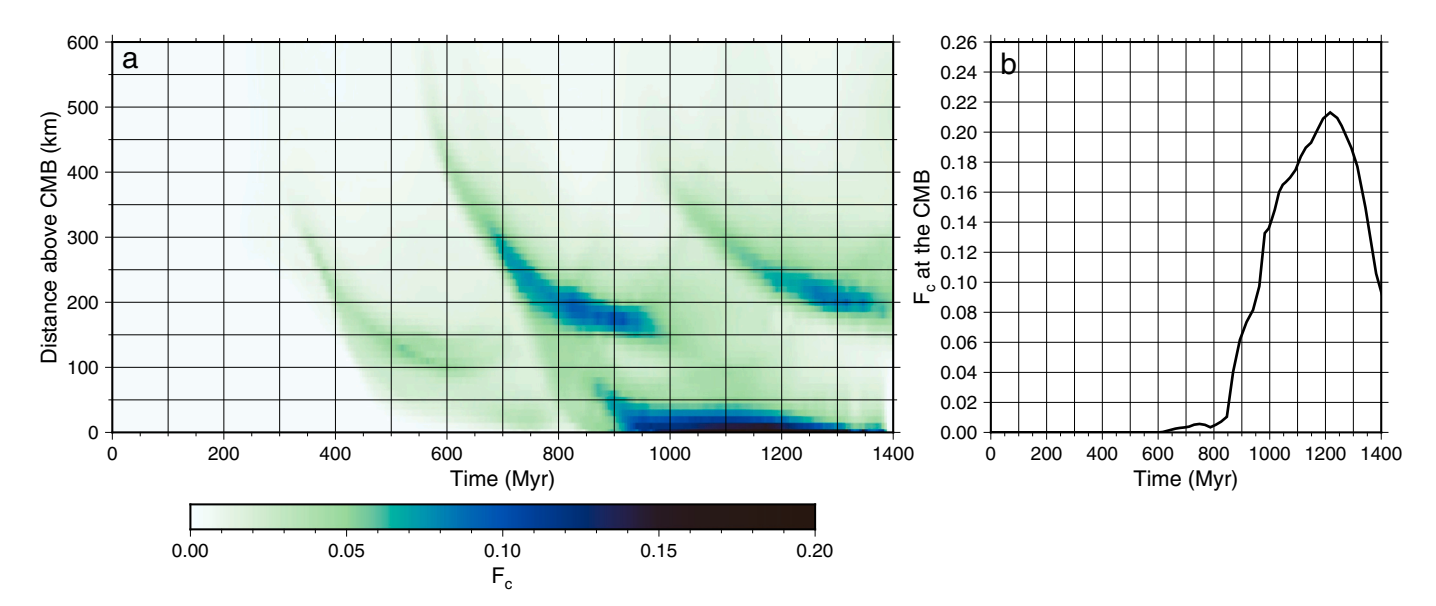


Fig. 4. Time evolution of crustal distribution in the lowermost mantle for case 1. a, areal fraction of model domain occupied by SOC, or F_C , at each depth in the lowermost 600 km of the mantle as a function of time. b, the areal fraction or F_C at the CMB (black) as a function of time.

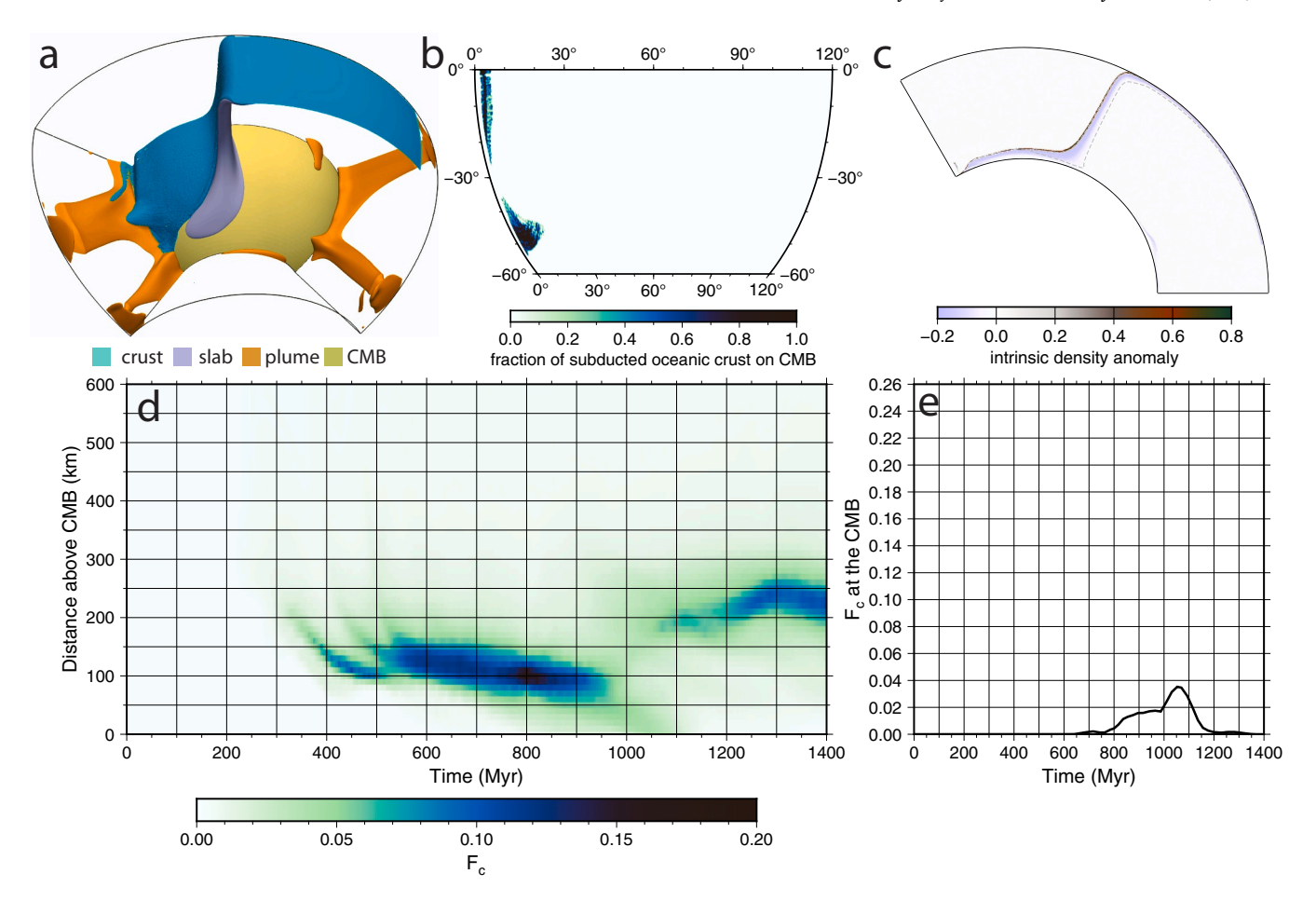


Fig. 5. a-c, same as panels (a-c) in Fig. 3 but for case 2 at 1115 Myr. d-e, the time evolution of the areal fraction of model domain occupied by SOC or F_C in the lowermost 600 km of the mantle (d), and the F_C at the CMB (e) for case 2.

<1% of the CMB area covered by SOC after \sim 600 Myr (Fig. 6e). In comparison to cases 1 and 2, where the SOC often concentrates at narrow depth ranges (Fig. 4a, 5d), the SOC in case 3 exhibits a wider depth distribution with a relatively lower concentration (Fig. 6d), possibly due to enhanced mixing in the lowermost mantle resulting from the presence of the weak pPv phase.

In case 4, the buoyancy numbers of both the MORB and harzburgite are set to zero; therefore, the SOC is only passively advected in the deep mantle. Compared to case 1, the dynamics of the subducted slab in case 4 is not significantly affected. In Figs. 7a-c, I show a snapshot of the temperature and composition fields of case 4 at 1050 Myr, which are very close to those in case 1 at approximately the same time as shown in Figs. 3g-i. The areal fraction of CMB covered by SOC in case 4 increases linearly from 0 at $\sim\!900$ Myr to a maximum of 0.15 at $\sim\!1100$ Myr and then decreases linearly with time (Fig. 7d-e), which is overall slightly smaller than that in case 1. Similar to case 1, there are strong temporal and spatial variations of the distribution of SOC at the CMB, within $\sim\!50$ km above the CMB, and at $\sim\!50\!-\!300$ km above the CMB, and the SOC on the CMB exhibits a variety of accumulation size and shapes with a variable degree of mixing with other mantle materials.

I also tested how the modeling results are affected by model resolution. Case 5 uses a model resolution that is twice lower than that of case 1, whereas other parameters are the same in both models. Specifically, case 5 has 384, 128, and 192 elements in the longitudinal, colatitudinal, and radial directions, respectively, resulting in a longitudinal resolution of \sim 19.0 km, a latitudinal resolution of \sim 29.0 km near the CMB, and a radial resolution of 15.0 km. The time evolution of the temperature and the compositional fields of case 5 is shown in Supplementary Information Movie S4. Compared to case 1, case 5 shows much

greater mixing between SOC with the background material, resulting in a lower fraction of SOC on the CMB (Fig. 8). However, both cases show the same behaviors of a subducted slab in the lowermost mantle, which extends laterally sometimes beneath the subducted plate and other times beneath the overriding plate. In both cases, the SOC is more easily segregated when the associated subducted slab is folded, resulting in the SOC being in the deepest portion of the slab and directly facing or in contact with the CMB. Furthermore, in both cases, the changing morphology of the subducted slab causes strong temporal and spatial variations in the distribution of SOC in the lowermost mantle, with variable degrees of mixing with other mantle materials.

4. Discussion

In this study, I perform 3D high resolution models with single-sided, asymmetric subduction to study the dynamics and distribution of SOC beneath subduction regions in the lowermost mantle. I find that the possibility for a thin layer of SOC to segregate from the associated subducted slab in the lowermost mantle is greatly controlled by the morphology of the subducted slab. After the subducted slab reaches the lowermost mantle, if it extends laterally beneath the overriding plate, the associated SOC occurs at the shallowest portion of the slab and is difficult to penetrate through. In this case, the SOC mainly exists at $\sim\!50\text{--}300\,$ km depths above the CMB until the slab is significantly warmed up when crustal segregation is more likely. In contrast, when the subducted slab is turned over and folded backward to beneath the subducting plate, the SOC can either be directly advected onto the CMB or first face the CMB and then segregate from the slab when the slab is warmed up. In this condition, the SOC mainly occurs at the CMB or

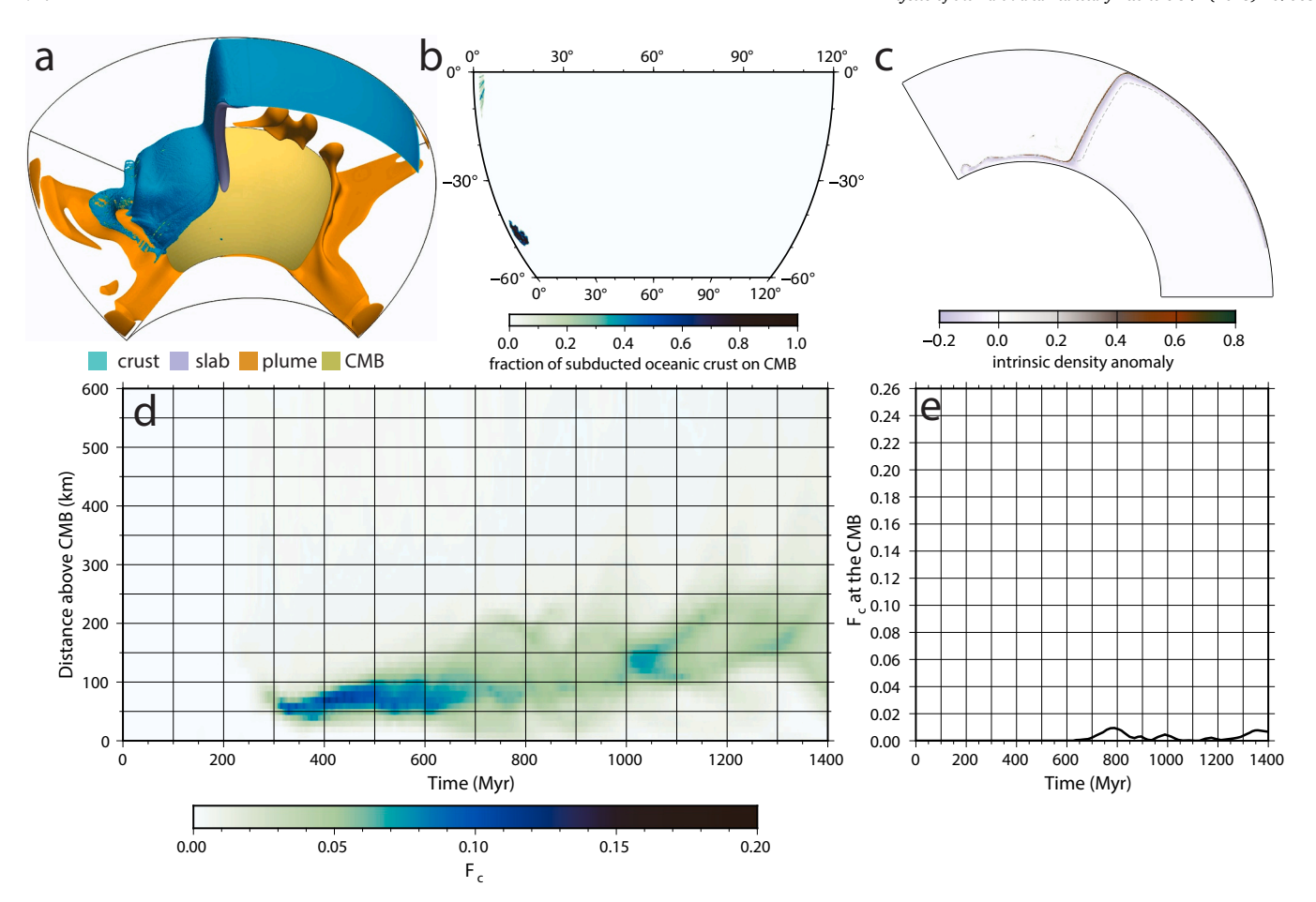


Fig. 6. a-c, same as panels (a-c) in Fig. 3 but for case 3 at 1013 Myr. d-e, the time evolution of the areal fraction of model domain occupied by SOC or F_C in the lowermost 600 km of the mantle (d), and the F_C at the CMB (e) for case 3.

within \sim 50 km above the CMB. In models where the subducted slab in the lowermost mantle switches between regions beneath the overriding plate and beneath the subducting plate, the SOC shows strong temporal changes of distribution between (1) regions at \sim 50–300 km above the CMB beneath the overriding plate, and (2) regions within \sim 50 km from the CMB beneath the subducting plate. Once SOC reaches the CMB, it migrates laterally along the CMB, exhibiting strong lateral variations in the concentration of crust and morphology of the crustal accumulation.

I find that the higher the viscosity contrast of the subducted slab with respect to the surrounding lowermost mantle, the more likely that the slab and its associated SOC will switch their distributions between regions beneath subducting plate and regions beneath overriding plate. In this study, I use the Frank-Kamenetskii approximation of the viscosity law with a maximum activation coefficient of E=11.51 which corresponds to a dimensional activation energy of ~240 kJ/mol. In laboratory experiments, the rheology of mantle materials is typically described by an Arrhenius viscosity law, in which the effects of temperature on viscosity are much more significant at lower temperatures than the Frank-Kamenetskii viscosity law, and it has a higher activation energy up to ~500 kJ/mol (Kohlstedt and Hansen, 2015). Therefore, if only considering the temperature-dependence of viscosity, the viscosity contrast of subducted slabs with respect to the background mantle in the Earth is likely higher than that in my models. If so, the modeling results suggest that subducted slabs in Earth's mantle could fold and switch between regions beneath subducting plates and regions beneath overriding plates, resulting in significant temporal and spatial variations in the distribution of SOC in the subduction-influenced regions outside the LLVPs. On the other hand, I find that the presence of weak pPv phase in the lowermost mantle may stabilize slab dynamics and cause them to consistently move in one direction in the lowermost mantle (Fig. 6, case 3). However, the extent to which the Bdg-pPv phase transition can cause a viscosity reduction remains a subject of debate, as well as the magnitude of this reduction (Hunt et al., 2009; Ammann et al., 2010; Karato, 2010). Furthermore, my models have limited size of model domain, so they do not consider the far-field effects from mantle convection outside the model domain. The most prominent structures in Earth's lowermost mantle are the two LLVPs. It has been suggested that the LLVPs (at least the one beneath Africa) may be unstable (Davaille, 1999; Yuan and Li, 2022a) and may have been rising in Earth's most recent history (Yuan and Li, 2022b). More work needs to be done to study how the interaction between the LLVPs and the subducted slabs in the lowermost mantle could affect the morphology of the subducted slabs.

I find that, compared to slab morphology, the segregation of a thin SOC is less affected by the intrinsic density anomaly of the SOC. The amount of crustal segregation on the CMB is only slightly reduced after removing the excess intrinsic density of SOC in case 4. The result indicates that although the SOC may be a few percent interictally denser than the background mantle, because the SOC is thin, its contribution to the buoyancy field and thus on the large-scale mantle flow field remains relatively small. Similar results have also been observed in our previous studies using 2D models (Li and McNamara, 2013; Li et al., 2014; Li and McNamara, 2022).

My results show that SOC at the side boundaries of the associated subducted slab is the easiest to segregate (e.g., Fig. 3h, 7b). This feature has been ignored in previous 2D models where the third dimension is assumed to be of infinite length. In Earth's mantle, the lengths of the trenches, and thus the subducted slabs, are limited. According to my

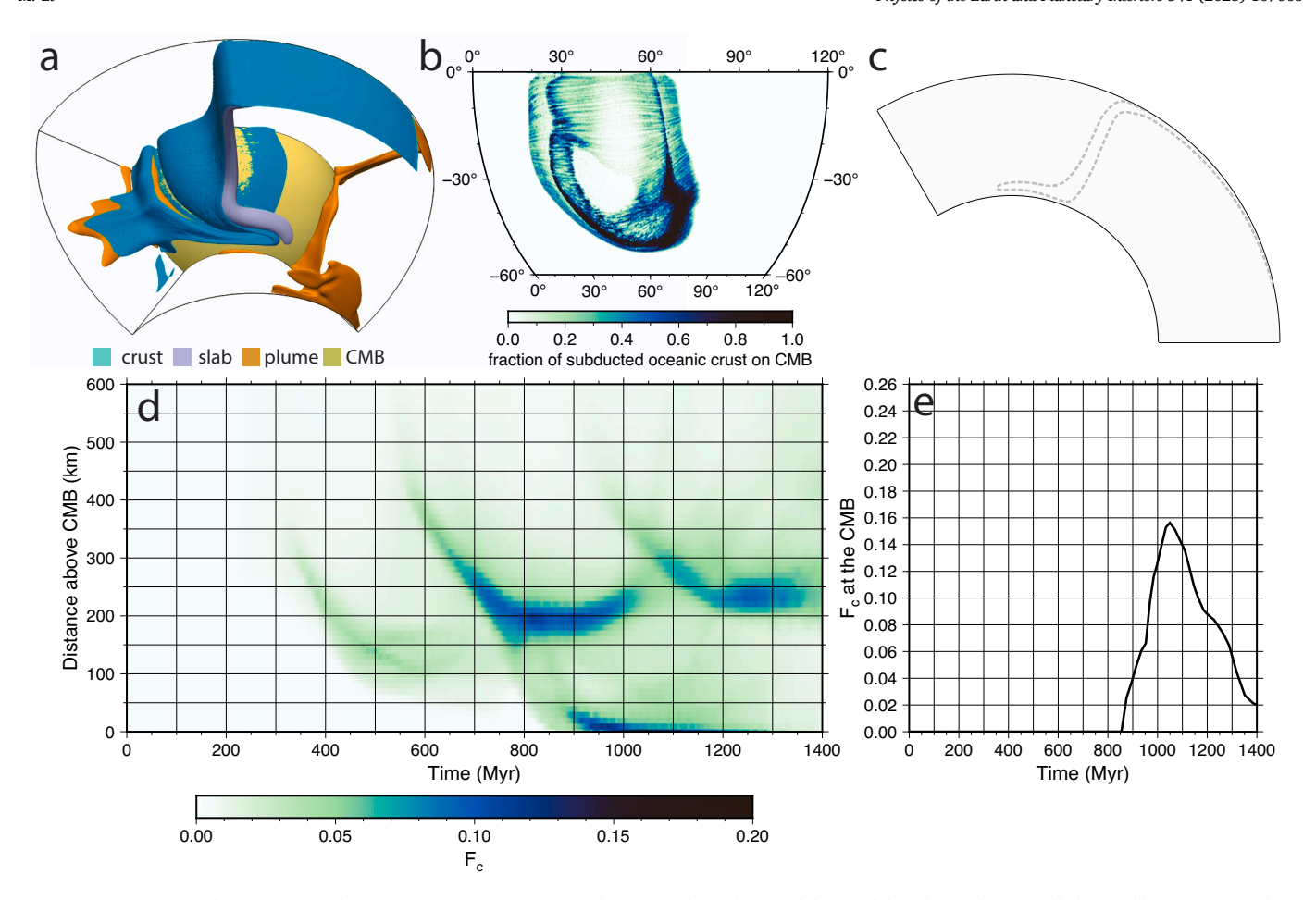


Fig. 7. a-c, same as panels (a-c) in Fig. 3 but for case 4 at 1050 Myr. Note that in panel c, only the subducted slab is shown, because all chemical heterogeneities have the same intrinsic density anomaly of zero. d-e, the time evolution of the areal fraction of model domain occupied by SOC or F_C in the lowermost 600 km of the mantle (d), and the F_C at the CMB (e) for case 4.

results, accumulations of SOC may preferentially occur at the side margins of the subducted slabs in the lowermost mantle. In addition, some subducted slabs contain gaps or holes (e.g., Sigloch et al., 2008; Obayashi et al., 2009; Harris et al., 2018; Portner and Hayes, 2018). My results suggest that segregation of SOC may preferentially occur in regions where the slabs contain gaps and holes in the lowermost mantle.

In my models, the subducted slabs sink with a speed of \sim 0.5–1.7 cm/ yr within the 660-2500 km depth range (Fig. 2c), which is consistent with previous estimations of the slab sinking rate of ~1.2 cm/yr based on interpretations of seismic tomography results (van der Meer et al., 2011). The buckling and folding behaviors of subducted slabs, as shown in this study, are also reported in previous geodynamic modeling studies (McNamara et al., 2002) and laboratory experiments (Loubet et al., 2009) and are observed by seismic studies as well (Hutko et al., 2006), suggesting that the modeling results in this study are relevant for the real Earth. Seismic studies have revealed wide-spread small-scale heterogeneities in the lowermost mantle outside the LLVPs, such as ultra-low velocity zones (ULVZs) (see review by Yu and Garnero, 2018), seismic scatterers (Frost et al., 2017), and other low velocity structures (Sun et al., 2013; He et al., 2014; Suzuki et al., 2016; Borgeaud et al., 2017; Nelson and Grand, 2018). Low velocity anomalies also appear in most global seismic tomography models, although their distribution vary between models (as summarized in Li, 2020). Importantly, seismic heterogeneities in the lowermost mantle outside the LLVPs show a large variety of shape, size, seismic velocity reductions, and density. In particular, as summarized by Yu and Garnero (2018), whereas ULVZs are confirmed in many regions such as beneath central America and western Pacific, there are also regions where no ULVZs are observed or,

at least, the ULVZs are too small or too thin to be observed with current techniques. Some of these seismic heterogeneities may be caused by temperature anomalies due to small-scale convection in the lowermost mantle (Li, 2020). Alternatively, they could be caused by compositional heterogeneities, especially the relatively small seismic anomalies and the kilometer-scale seismic scatterers. My models show that the subduction of even a single slab to the lowermost mantle could lead to strong temporal and spatial variations in crustal distribution beneath the subduction zone at the CMB, within 50 km of the CMB, and at \sim 50–300 km depths above the CMB. While migrating along the CMB, the SOC mixes with other materials and takes on different shapes. Mineral physics experiments and first-principle calculations have shown that SOC has different seismic velocities (Stixrude and Lithgow-Bertelloni, 2012; Thomson et al., 2019; Wang et al., 2020), reduced melting temperature (Andrault et al., 2014), and increased intrinsic density (e.g., Ringwood and Irifune, 1988; Kesson et al., 1994; Hirose et al., 2005; Ricolleau et al., 2010; Tsuchiya, 2011) than a pyrolite background mantle. Therefore, I infer that the temporal and spatial variations of the distribution of SOC which has unique physical properties could cause large variations of seismic velocities, density, morphology, and distribution of the wide-spread seismic anomalies in the lowermost mantle outside the LLVPs. This inference can be further tested by converting the temperature and compositional fields of geodynamic models into seismic velocities in future research.

Finally, it has been suggested that modern style plate tectonics may have begun at $\sim 3.0~Ga$ (see review by Condie, 2018). In this case, more slab buckling and folding events may have occurred in Earth's history than those shown in my models. Although the subduction process in

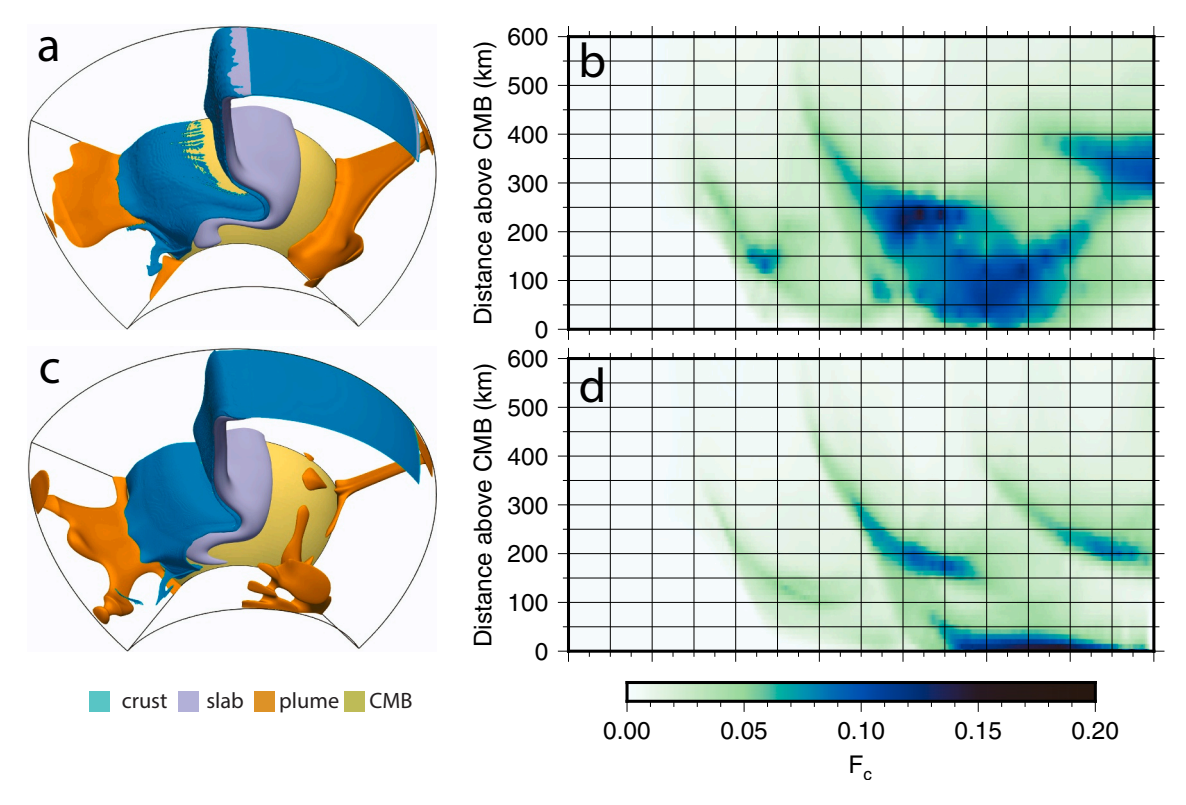


Fig. 8. a, snapshots of temperature and composition fields for case 5 at 842 Myr. Cyan color shows regions where the fraction of oceanic crust is larger than 0.3, blueish color shows a subducted slab by the temperature isosurface of T=0.435, orange color shows mantle plumes as the isosurface of the temperature anomaly (after removing the lateral average temperature) at 0.15, and green color shows the CMB. b, the time evolution of the areal fraction of model domain occupied by SOC or F_C in the lowermost 600 km of the mantle. c, same as panel (a) but for case 1 at 869 Myr. d, same as panel (b) but for case 1.

Earth's most recent history may primarily affect the chemical heterogeneities in Earth's lowermost mantle beneath regions of subduction outside the LLVPs, the continuous subduction process during the past several billions of years could bring a significant amount of SOC into Earth's deep mantle. Some of the SOC may accumulate as thermochemical piles on the CMB, contributing to the composition of the LLVPs (Jones et al., 2020; Li and McNamara, 2022), and some may be entrained to shallower depths where they may mix with other compositional components (Li and McNamara, 2013) or become partially molten in mantle plumes beneath hotspots and large-igneous provinces (Sobolev et al., 2007; Li et al., 2014; Dannberg and Sobolev, 2015; Li, 2021).

5. Conclusion

In this study, I perform 3D high-resolution geodynamic models with single-sided, asymmetric subduction to study the dynamics of subducted slabs in the lowermost mantle beneath subduction regions. I find that the morphology of a subducted slab in the lowermost mantle greatly controls the ability for the associated subducted oceanic crust (SOC) to segregate and determines its distribution. When the slab extends beneath the overriding plate, the crust occurs at the topmost of the slab and is difficult to penetrate through, resulting in most of the crust being distributed at \sim 50–300 km above the CMB. However, when the slab is folded backward and extends beneath the subducting plate, the crust appears at the deepest part of the slab and can easily segregate onto the CMB. Crustal segregation also preferentially occurs at the lateral edges of the subducted slab in the lowermost mantle. In the lowermost mantle, a slab with high viscosity can undergo folding and redistribution, shifting between the region beneath the subducting plate and the region beneath the overriding plate. While migrating along the CMB, the SOC is shaped into accumulations with variable sizes and shapes and shows different degrees of mixing with the background material. As a result,

the SOC shows strong temporal and spatial variations at the CMB, within $\sim\!50\,\mathrm{km}$ above the CMB, and at $\sim\!50\text{--}300\,\mathrm{km}$ above the CMB. Given that SOC has different composition, seismic velocities, intrinsic density, and melting temperature than the pyrolite background mantle, my results suggest that the large variation of seismic velocities, density, size, shape, and distribution of the wide-spread seismic heterogeneities in the lowermost mantle outside the LLVPs may be explained by SOC.

Supplementary data to this article can be found online at https://doi.org/10.1016/j.pepi.2023.107063.

CRediT authorship contribution statement

Mingming Li: Conceptualization, Methodology, Investigation, Visualization, Funding acquisition, Project administration, Writing - original draft, Writing - review & editing.

Declaration of Competing Interest

Mingming Li reports financial support, administrative support, article publishing charges, equipment, or supplies, and travel were provided by National Science Foundation.

Data availability

The code is open source. I have provided a link for the code in the Acknowledgements section.

Acknowledgements

This work is supported by NSF grants EAR-2216564, EAR-2054926, and EAR-1855624. There is no conflict of interests. The CitcomCU code used in this work is open source and is available at http://geoweb.cse.ucdavis.edu/cig/software/citcomcu/.

References

- Ammann, M.W., Brodholt, J.P., Wookey, J., Dobson, D.P., 2010. First-principles constraints on diffusion in lower-mantle minerals and a weak D' layer. Nature 465, 462, 465
- Andrault, D., Pesce, G., Bouhifd, M.A., Bolfan-Casanova, N., Hénot, J.-M., Mezouar, M., 2014. Melting of subducted basalt at the core-mantle boundary. Science 344, 892–895
- Borgeaud, A.F.E., Kawai, K., Konishi, K., Geller, R.J., 2017. Imaging paleoslabs in the D" layer beneath Central America and the Caribbean using seismic waveform inversion. Sci. Adv. 3, e1602700.
- Brandenburg, J.P., van Keken, P.E., 2007. Deep storage of oceanic crust in a vigorously convecting mantle. J. Geophys. Res. 112, B06403.
- Christensen, U.R., Hofmann, A.W., 1994. Segregation of subducted oceanic crust in the convecting mantle. J. Geophys. Res. 99, 19867–19884.
- Čížková, H., Bina, C.R., 2019. Linked influences on slab stagnation: interplay between lower mantle viscosity structure, phase transitions, and plate coupling. Earth Planet. Sci. Lett. 509, 88–99.
- Condie, K.C., 2018. A planet in transition: the onset of plate tectonics on Earth between 3 and 2 Ga? Geosci. Front. 9, 51–60.
- Crameri, F., Tackley, P.J., 2015. Parameters controlling dynamically self-consistent plate tectonics and single-sided subduction in global models of mantle convection. J. Geophys. Res. 120, 3680–3706.
- Dannberg, J., Sobolev, S.V., 2015. Low-buoyancy thermochemical plumes resolve controversy of classical mantle plume concept. Nat. Commun. 6, 6960.
- Davaille, A., 1999. Simultaneous generation of hotspots and superswells by convection in a heterogenous planetary mantle. Nature 402, 756–760.
- Davies, G.F., 2008. Episodic layering of the early mantle by the 'basalt barrier' mechanism. Earth Planet. Sci. Lett. 275, 382–392.
- Davies, D.R., Davies, J.H., 2009. Thermally-driven mantle plumes reconcile multiple hotspot observations. Earth Planet. Sci. Lett. 278, 50–54.
- Frank-Kamenetskii, D.A., 1969. Diffusion and Heat Transfer in Chemical Kinetics.
 Plenum Press.
- Frost, D.A., Rost, S., Garnero, E.J., Li, M., 2017. Seismic evidence for Earth's crusty deep mantle. Earth Planet. Sci. Lett. 470, 54–63.
- Fukao, Y., Obayashi, M., 2013. Subducted slabs stagnant above, penetrating through, and trapped below the 660 km discontinuity. J. Geophys. Res. 118, 5920–5938.
- Fukao, Y., Obayashi, M., Nakakuki, T., Grp, D.S.P., 2009. Stagnant slab: a review. Annu. Rev. Earth Planet. Sci. 37, 19–46.
- Garnero, E.J., McNamara, A.K., Shim, S.-H., 2016. Continent-sized anomalous zones with low seismic velocity at the base of Earth's mantle. Nat. Geosci. 9, 481–489.
- Grand, S.P., 2002. Mantle shear-wave tomography and the fate of subducted slabs. Philosophical Transactions of the Royal Society of London Series a-Mathematical Physical and Engineering Sciences 360, 2475–2491.
- Grand, S.P., van der Hilst, R.D., Widiyantoro, S., 1997. Global seismic tomography: a snapshot of convection in the earth. GSA Today 7, 1–7.
- Gurnis, M., 1986. The effects of chemical density differences on convective mixing in the earths mantle. J Geophys Res-Solid 91, 1407–1419.
- Hansen, S.E., Garnero, E.J., Li, M., Shim, S.-H., Rost, S., 2023. Globally distributed subducted materials along the Earth's core-mantle boundary: Implications for ultralow velocity zones. Sci. Adv. 9, eadd4838.
- Harris, C.W., Miller, M.S., Porritt, R.W., 2018. Tomographic imaging of slab segmentation and deformation in the greater Antilles. Geochem. Geophys. Geosyst. 19, 2292–2307.
- He, Y., Wen, L., Zheng, T., 2014. Seismic evidence for an 850-km thick low-velocity structure in the Earth's lowermost mantle beneath Kamchatka. Geophys. Res. Lett. 41, 7073–7079.
- Hirose, K., Takafuji, N., Sata, N., Ohishi, Y., 2005. Phase transition and density of subducted MORB crust in the lower mantle. Earth Planet. Sci. Lett. 237, 239–251.
- Hofmann, A.W., White, W.M., 1982. Mantle plumes from ancient oceanic-crust. Earth Planet. Sci. Lett. 57, 421–436.
- Huang, J.S., Davies, G.F., 2007. Geochemical processing in a three-dimensional regional spherical shell model of mantle convection. Geochem. Geophys. Geosyst. 8, Q11006.
- Hunt, S.A., Weidner, D.J., Li, L., Wang, L.P., Walte, N.P., Brodholt, J.P., Dobson, D.P., 2009. Weakening of calcium iridate during its transformation from perovskite to post-perovskite. Nat. Geosci. 2, 794–797.
- Hutko, A.R., Lay, T., Garnero, E.J., Revenaugh, J., 2006. Seismic detection of folded, subducted lithosphere at the core–mantle boundary. Nature 441, 333–336.
- Jones, T.D., Maguire, R.R., van Keken, P.E., Ritsema, J., Koelemeijer, P., 2020. Subducted oceanic crust as the origin of seismically slow lower-mantle structures. Progress in Earth and Planetary Science 7, 17.
- Karato, S., 2010. The influence of anisotropic diffusion on the high-temperature creep of a polycrystalline aggregate. Phys. Earth Planet. Inter. 183, 468–472.
- Kesson, S.E., Fitz Gerald, J.D., Shelley, J.M.G., 1994. Mineral chemistry and density subducted basaltic crust at lower-mantle pressures. Nature 372, 767–769.
- King, S.D., Gable, C.W., Weinstein, S.A., 1992. Models of convection-driven tectonic plates: a comparison of methods and results. Geophys. J. Int. 109, 481–487.
- Kohlstedt, D.L., Hansen, L.N., 2015. 2.18 constitutive equations, rheological behavior, and viscosity of rocks. In: Schubert, G. (Ed.), Treatise on Geophysics (Second Edition). Elsevier, Oxford, pp. 441–472.
- Li, M., 2020. The formation of hot thermal anomalies in cold subduction-influenced regions of Earth's lowermost mantle. J. Geophys. Res. 125 (e2019JB019312).
- Li, M., 2021. The cycling of subducted oceanic crust in the Earth's deep mantle. Mantle Convection and Surface Expressions 303–328.
- Li, M., McNamara, A.K., 2013. The difficulty for subducted oceanic crust to accumulate at the Earth's core-mantle boundary. J. Geophys. Res. 118, 1807–1816.

- Li, M., McNamara, A.K., 2022. Evolving morphology of crustal accumulations in Earth's lowermost mantle. Earth Planet. Sci. Lett. 577, 117265.
- Li, X.D., Romanowicz, B., 1996. Global mantle shear velocity model developed using nonlinear asymptotic coupling theory. J. Geophys. Res. 101, 22245–22272.
- Li, C., van der Hilst, R.D., Engdahl, E.R., Burdick, S., 2008. A new global model for P wave speed variations in Earth's mantle. Geochem. Geophys. Geosyst. 9
- Li, M., McNamara, A.K., Garnero, E.J., 2014. Chemical complexity of hotspots caused by cycling oceanic crust through mantle reservoirs. Nat. Geosci. 7, 366–370.
- Loubet, N., Ribe, N.M., Gamblin, Y., 2009. Deformation modes of subducted lithosphere at the core-mantle boundary: an experimental investigation. Geochem. Geophys. Geosyst. 10, Q10004.
- Lowman, J.P., 2011. Mantle convection models featuring plate tectonic behavior: an overview of methods and progress. Tectonophysics 510, 1–16.
- Lowman, J.P., King, S.D., Gable, C.W., 2004. Steady plumes in viscously stratified, vigorously convecting, three-dimensional numerical mantle convection models with mobile plates. Geochem. Geophys. Geosyst. 5, Q01L01.
- McNamara, A.K., 2019. A review of large low shear velocity provinces and ultra low velocity zones. Tectonophysics 760, 199–220.
- McNamara, A.K., van Keken, P.E., Karato, S.-I., 2002. Development of anisotropic structure in the Earth's lower mantle by solid-state convection. Nature 416, 310–314.
- McNamara, A.K., Garnero, E.J., Rost, S., 2010. Tracking deep mantle reservoirs with ultra-low velocity zones. Earth Planet. Sci. Lett. 299, 1–9.
- Mulyukova, E., Steinberger, B., Dabrowski, M., Sobolev, S.V., 2015. Survival of LLSVPs for billions of years in a vigorously convecting mantle: replenishment and destruction of chemical anomaly. J. Geophys. Res. 120, 3824–3847.
- Nakagawa, T., Tackley, P.J., 2014. Influence of combined primordial layering and recycled MORB on the coupled thermal evolution of Earth's mantle and core. Geochem. Geophys. Geosyst. 15, 619–633.
- Nelson, P.L., Grand, S.P., 2018. Lower-mantle plume beneath the Yellowstone hotspot revealed by core waves. Nat. Geosci. 11, 280–284.
- Obayashi, M., Yoshimitsu, J., Fukao, Y., 2009. Tearing of stagnant slab. Science 324, 1173–1175.
- Portner, D.E., Hayes, G.P., 2018. Incorporating teleseismic tomography data into models of upper mantle slab geometry. Geophys. J. Int. 215, 325–332.
- Ricolleau, A., Perrillat, J.-P., Fiquet, G., Daniel, I., Matas, J., Addad, A., Menguy, N., Cardon, H., Mezouar, M., Guignot, N., 2010. Phase relations and equation of state of a natural MORB: implications for the density profile of subducted oceanic crust in the Earth's lower mantle. J. Geophys. Res. 115, B08202.
- Ringwood, A.E., Irifune, T., 1988. Nature of the 650-km seismic discontinuity: implications for mantle dynamics and differentiation. Nature 331, 131-136.
- Ritsema, J., van Heijst, H.J., Woodhouse, J.H., 2004. Global transition zone tomography. J. Geophys. Res. 109, B02302.
- Ritsema, J., Deuss, A., van Heijst, H.J., Woodhouse, J.H., 2011. S40RTS: a degree-40 shear-velocity model for the mantle from new Rayleigh wave dispersion, teleseismic traveltime and normal-mode splitting function measurements. Geophys. J. Int. 184, 1223–1236.
- Shim, S.-H., 2008. The Postperovskite transition. Annu. Rev. Earth Planet. Sci. 36, 569–599.
- Sigloch, K., Mcquarrie, N., Nolet, G., 2008. Two-stage subduction history under North America inferred from multiple-frequency tomography. Nat. Geosci. 1, 458–462.
- Sobolev, A.V., Hofmann, A.W., Kuzmin, D.V., Yaxley, G.M., Arndt, N.T., Chung, S.L., Danyushevsky, L.V., Elliott, T., Frey, F.A., Garcia, M.O., Gurenko, A.A., Kamenetsky, V.S., Kerr, A.C., Krivolutskaya, N.A., Matvienkov, V.V., Nikogosian, I. K., Rocholl, A., Sigurdsson, I.A., Sushchevskaya, N.M., Teklay, M., 2007. The amount of recycled crust in sources of mantle-derived melts. Science 316, 412–417.
- Steinberger, B., Calderwood, A.R., 2006. Models of large-scale viscous flow in the Earth's mantle with constraints from mineral physics and surface observations. Geophys. J. Int. 167, 1461–1481.
- Stixrude, L., Lithgow-Bertelloni, C., 2012. Geophysics of chemical heterogeneity in the mantle. Annu. Rev. Earth Planet. Sci. 40, 569–595.
- Sun, D., Helmberger, D.V., Jackson, J.M., Clayton, R.W., Bower, D.J., 2013. Rolling hills on the core-mantle boundary. Earth Planet. Sci. Lett. 361, 333–342.
- Suzuki, Y., Kawai, K., Geller, R.J., Borgeaud, A.F.E., Konishi, K., 2016. Waveform inversion for 3-D S-velocity structure of D" beneath the northern Pacific: possible evidence for a remnant slab and a passive plume. Earth, Planets and Space 68, 198.
- Tackley, P.J., 2000. Self-consistent generation of tectonic plates in time-dependent, three-dimensional mantle convection simulations. Geochem. Geophys. Geosyst. 1, 1021.
- Tackley, P.J., 2011. Living dead slabs in 3-D: the dynamics of compositionally-stratified slabs entering a "slab graveyard" above the core-mantle boundary. Phys. Earth Planet. Inter. 188, 150–162.
- Tackley, P.J., King, S.D., 2003. Testing the tracer ratio method for modeling active compositional fields in mantle convection simulations. Geochem. Geophys. Geosyst. 4, 8302.
- Tan, E., Gurnis, M., Han, L., 2002. Slabs in the lower mantle and their modulation of plume formation. Geochem. Geophys. Geosyst. 3, 1–24.
- Thomson, A.R., Crichton, W.A., Brodholt, J.P., Wood, I.G., Siersch, N.C., Muir, J.M.R., Dobson, D.P., Hunt, S.A., 2019. Seismic velocities of CaSiO3 perovskite can explain LLSVPs in Earth's lower mantle. Nature 572, 643–647.
- Tolstikhin, I., Hofmann, A.W., 2005. Early crust on top of the Earth's core. Phys. Earth Planet. Inter. 148, 109–130.
- Tsuchiya, T., 2011. Elasticity of subducted basaltic crust at the lower mantle pressures: insights on the nature of deep mantle heterogeneity. Phys. Earth Planet. Inter. 188, 142–149.

- van der Meer, D.G., Spakman, W., van Hinsbergen, D.J.J., Amaru, M.L., Torsvik, T.H., 2011. Towards absolute plate motions constrained by lower-mantle slab remnants. Nat. Geosci. 3, 36–40.
- Wang, Y., Li, M., 2020. Constraining mantle viscosity structure from a statistical analysis of slab stagnation events. Geochem. Geophys. Geosyst. 21 (e2020GC009286).
- Wang, W., Xu, Y., Sun, D., Ni, S., Wentzcovitch, R., Wu, Z., 2020. Velocity and density characteristics of subducted oceanic crust and the origin of lower-mantle heterogeneities. Nat. Commun. 11, 64.
- Yoshioka, S., Naganoda, A., 2010. Effects of trench migration on fall of stagnant slabs into the lower mantle. Phys. Earth Planet. Inter. 183, 321–329.
- Yu, S.L., Garnero, E.J., 2018. Ultralow velocity zone locations: a global assessment. Geochem. Geophys. Geosyst. 19, 396–414.
- Yuan, Q., Li, M., 2022a. Instability of the African large low-shear-wave-velocity province due to its low intrinsic density. Nat. Geosci. 15, 334–339.
- Yuan, Q., Li, M., 2022b. Vastly Different Heights of LLVPs caused by different strengths of historical slab push. Geophys. Res. Lett. 49 (e2022GL099564).
- Zhong, S., 2006. Constraints on thermochemical convection of the mantle from plume heat flux, plume excess temperature, and upper mantle temperature. J. Geophys. Res. 111, B04409.